JM PAPERS

The minimal flow unit and origin of two-dimensional elasto-inertial turbulence

Hongna Zhang[1], Haotian Cheng[1], Suming Wang[1], Wenhua Zhang[1],†, Xiaobin Li[1] and Fengchen Li[1]

[1]State Key Laboratory of Engine, Tianjin University, Tianjin 300350, PR China

The research on elasto-inertial turbulence (EIT), a new type of turbulent flow, has reached the stage of identifying the minimal flow unit (MFU). On this issue, direct numerical simulations of FENE-P fluid flow in two-dimensional channels with variable sizes are conducted in this study. We demonstrate with the increase of channel length that the simulated flow experiences several different flow patterns, and there exists an MFU for EIT to be self-sustained. At Weissenberg number (*Wi*) higher than the one required to excite EIT, when the channel length is relatively small, a steady arrowhead regime (SAR) flow structure and a laminar-like friction coefficient is achieved. However, as the channel length increases, the flow can fully develop into EIT characterized with high flow drag. Close to the size of the MFU, the simulated flow behaves intermittently between the SAR state with low drag and EIT state with high drag. The flow falling back to 'laminar flow' is caused by the insufficient channel size below the MFU. Furthermore, we give the relationship between the value of the MFU and the effective *Wi*, and explain its physical reasons. Moreover, the intermittent flow regime obtained based on the MFU gives us an opportunity to look into the origin and exciting process of EIT. Through capturing the onset process of EIT, we observed that EIT originates from the sheet-like extension structure located near the wall, which is maybe related to the wall mode rather than the centre mode. The fracture and regeneration of this sheet-like structure is the key mechanism for the self-sustaining of EIT.

Key words: viscoelasticity, turbulence simulation, turbulence theory

1. Introduction

Viscoelastic fluids widely exist in nature, and their unique rheological properties give rise to different flow behaviours comparing with Newtonian fluids, such as the drag-reducing turbulence (DRT) (Toms 1949; White & Mungal 2008; Li *et al.* 2012) at a moderate or high

† Email address for correspondence: zhangwh2022@tju.edu.cn

Reynolds number (*Re*), and elastic turbulence (ET) (Groisman & Steinberg 2000, 2004; Steinberg 2021) at an extremely low *Re*. The recent discovery of a new type of turbulent state (elasto-inertial turbulence, EIT) by Samanta *et al.* (2013) opened up new avenues for viscoelastic turbulence. Unlike Newtonian inertial turbulence (IT) and ET, EIT arises from the combined effects of nonlinear elasticity and flow inertia. Its distinctive characteristics are trains of spanwise cylindrical vortex structures of alternating sign around sheets of high polymer extension (Dubief, Terrapon & Julio 2013; Choueiri, Lopez & Hof 2018; Shekar *et al.* 2019). The understanding of EIT has provided valuable insights into the maximum drag reduction state of DRT as well as the early turbulence of viscoelastic fluids (Dubief, Terrapon & Hof 2023).

The origin and self-sustaining mechanisms of EIT are hot topics, with the investigations focusing on whether it originates from wall-mode (Tollmien–Schlichting (TS) mode) or centre-mode instability, as well as arising from a subcritical or supercritical transition (Sánchez *et al.* 2022; Dubief *et al.* 2023). Here, the wall mode and centre mode are characterized as propagating at a phase speed close to the critical-layer velocity near the channel wall, and the base state maximum velocity at the channel centre, respectively. On the one hand, through linear stability analysis, Garg *et al.* (2018) and Khalid *et al.* (2021) discovered the linear instability of centre mode under high *Wi* in pipe and channel flow, respectively. The existence of centre-mode instability can provide a dynamic origin of EIT Beneitez *et al.* (2024). Weakly nonlinear analysis by Wan, Sun & Zhang (2021) indicated that the transition to EIT is subcritical at low polymer concentrations, and supercritical at high polymer concentrations. Numerical simulations revealed that the subcritical nonlinear evolution of the centre mode can induce saturated 'arrowhead' travelling waves (Page, Dubief & Kerswell 2020), which exhibits the arrowhead structure (the landmark of centre mode) and can become a stable attractor for EIT dynamics at sufficiently large *Wi*. Four coexistent attractors – e.g. steady arrowhead regime (SAR) and chaotic arrowhead regime – were identified by Dubief *et al.* (2022) and Beneitez *et al.* (2024), supporting the idea of linear instability. In the experiments of viscoelastic pipe flow (Choueiri *et al.* 2021), similar arrowhead structures of centre mode were observed at low *Re*, suggesting the significance of centre-mode instability in the origin of EIT. On the other hand, some researchers argued that the mechanism of EIT induced by the wall-mode instability is closely related to the excitation of TS waves. The Graham group proposed the critical layer theory and the nonlinear routine to EIT induced by TS mode (wall mode) in plane Poiseuille flow for low *Wi* (Shekar *et al.* 2019, 2020, 2021). They found two kinds of TS attractors linked to EIT: a viscoelastic nonlinear TS attractor (VNTSA) and a Newtonian TS attractor. At moderate *Re*, although similar to the stable Newtonian TS mode, a VNTSA can be connected to two-dimensional (2-D) EIT through an unstable solution branch (Shekar *et al.* 2020). At high *Re*, the unstable Newtonian TS attractor can evolve continuously into an EIT state as *Wi* increases (Shekar *et al.* 2021). Therefore, they argued that the wall mode (or TS mode) and critical layer play a key role in the onset process of EIT. A similar viewpoint is also obtained by Beneitez *et al.* (2024), who pointed out that the chaotic dynamics of EIT is a wall-focused phenomenon.

So far, researches on the origin and mechanism of EIT have yielded many insightful findings, but the picture is still incomplete and numerous questions remain open. Direct numerical simulations (DNS) can shed crucial light on these questions. However, the numerical criterion that is well-documented for Newtonian IT has not yet been

established for EIT. The well-known high Weissenberg number problem (HWNP) has long bottlenecks in the simulations of high-*Wi* viscoelastic fluid flows, especially EIT and ET. Although great efforts have been made in dealing with the HWNP over the past two decades, it has not been completely solved (Alves, Oliveira & Pinho 2021). Many of the numerical studies on EIT adopt some artificial diffusion to alleviate the hyperbolicity of the constitutive model at high *Wi*, which is often considered as one of the main causes of the HWNP. The addition of an artificial diffusion term can stabilize the numerical simulations of high-*Wi* viscoelastic fluid flows in a way, but at the cost of numerical accuracy. Moreover, recently it was demonstrated that the presence of non-zero diffusivity of the polymer stress can change the flow stability of Oldroyd-B and FENE-P fluid by inducing a new mechanism of linear instability, i.e. polymer diffusive instability (PDI) (Beneitez, Page & Kerswell 2023); this can also lead to a self-sustaining chaotic state, and the inertia can enhance its prevalence comparing with the cases in the inertialess limit (Couchman *et al.* 2024). These important findings indicate that in numerical simulations, PDI could also be a possible trigger of ET and EIT for Oldroyd-B and FENE-P fluids, which, however, is non-physical. Therefore, avoiding the PDI by suitable numerical methods is also a necessity to establish the numerical criterion for EIT as well as ET.

In addition to the numerical methods, the size of the computational domain is also a key factor to excite and sustain turbulence, which also lacks of systematic investigation for EIT. The improper choice of computational domain sometimes leads to a different picture of dominant dynamics. For example, as reported in Dubief *et al.* (2022), the simulated flow states are related to the computational domain, and an increase in the streamwise length can change the SAR state to the EIT state under the same parameters. Zhu & Xi (2021) obtained slightly higher friction factors after enlarging the computational domain, explained as spatial intermittency and correlation on longer length scales. In our previous studies on EIT of Oldroyd-B fluids (Zhang *et al.* 2022), we found that a longer channel is required to excite EIT as *Wi* increases. Therefore, a standard numerical criterion for DNS of EIT after solving the HWNP is a prior and plays a crucial role in drawing a complete picture of EIT dynamics.

To establish this criterion, it is worth emphasizing the importance of finding the minimal flow unit (MFU) that can ensure the occurrence and continuous self-sustenance of turbulence (Jiménez & Moin 1991). In numerical simulations of turbulence, it is commonly required to ensure that the computational domain is sufficiently long to allow for adequate turbulence development, and that the streamwise correlation reaches zero within half of the domain length (Dubief *et al.* 2023). The statistical results based on the MFU agree with those obtained from significantly larger flow units. The use of the MFU provides reliable guidance for selecting the computational domain size in numerical simulations, ensuring that the results contain complete and accurate physical information while reducing the computational cost associated with large domains. It has played an important role in understanding the self-sustaining mechanisms of turbulent structures therein, and has remained widely employed in studies related to Newtonian wall-bounded turbulence (Yin, Huang & Xu 2018). However, few studies are conducted on the MFU of viscoelastic turbulence, particularly EIT. Xi & Graham (2010) explored the MFU for DRT in three-dimensional channel flow. Later, Graham (2014) mentioned that the Newtonian fluid MFU cannot sustain turbulence at high *Wi*. Like Newtonian IT, the MFU is also a necessity to further promote the understanding of EIT, including the self-sustaining process of coherent structures, exact coherent structures, and so on.

Against the above backdrop, this paper aims to find the size of MFU that is able to sustain EIT, thereby discussing its origin. To this end, a comprehensive investigation on the computational domain effects on the flow characteristics in a wide range of parameters is required, based on reliable numerical methods. In our recent work, we identified the improper interpolation of the tensor field when solving the constitutive equations as the main cause of the HWNP (Zhang *et al.* 2023). Instead of component-based interpolation, we proposed a tensor-based interpolation method for the conformation tensor field, and have demonstrated the effectiveness of the tensor-based interpolation method in resolving the challenges of the HWNP with no need for an artificial diffusion term. This efficient and stable numerical method offers us the ability to access the numerical criterion of EIT today. Moreover, the 2-D nature of EIT demonstrated by Sid, Terrapon & Dubief (2018) implies that the MFU of EIT in a channel is determined mainly by the streamwise length of the computational domain. Therefore, we conduct a series of numerical simulations on 2-D plane Poiseuille flow to find the MFU suitable for EIT, and thereby explore its origin. The remaining sections are organized as follows. Section 2 introduces the governing equations of viscoelastic fluid flow, numerical methods and conditions. Section 3 discusses the computational domain effects on flow characteristics and explores the origin of EIT based on its MFU. Section 4 gives the conclusions.

2. Numerical methodology

2.1. *Governing equations*

This study focuses on the 2-D plane Poiseuille flows of FENE-P fluid under a constant flow rate. Channel walls are assumed to be no-slip, and the periodic boundary condition is applied in the streamwise direction. The channel half-height h, the bulk mean velocity u_b, h/u_b, and ρu_b^2 are chosen as the reference length, velocity, time and pressure, respectively. Here, ρ is the fluid density, and $u_b = (1/2h) \int_0^{2h} \bar{u}(y)\, \mathrm{d}y$, with $\bar{u}(y)$ the locally averaged velocity in the streamwise direction, and an overline indicates an ensemble-averaged variable. Then the dimensionless governing equations of FENE-P fluid flow in the form of the conformation tensor c are as follows:

$$\nabla \cdot \boldsymbol{u} = 0, \tag{2.1}$$

$$\frac{\partial \boldsymbol{u}}{\partial t} + \boldsymbol{u} \cdot \nabla \boldsymbol{u} = -\nabla p + \frac{\beta}{Re} \nabla^2 \boldsymbol{u} + \nabla \cdot \boldsymbol{\tau}_p, \tag{2.2}$$

$$\boldsymbol{\tau}_p = \frac{1-\beta}{Re\, Wi} [f(r)\, \boldsymbol{c} - \boldsymbol{I}], \tag{2.3}$$

$$\frac{\partial \boldsymbol{c}}{\partial t} + (\boldsymbol{u} \cdot \nabla)\boldsymbol{c} - \boldsymbol{c} \cdot (\nabla \boldsymbol{u}) - (\nabla \boldsymbol{u})^{\mathrm{T}} \cdot \boldsymbol{c} = -\frac{f(r)\, \boldsymbol{c} - \boldsymbol{I}}{Wi}, \tag{2.4}$$

where $\boldsymbol{u}$ is the velocity vector, with (u, v) denoting the streamwise (x) and normal (y) direction velocity components. Here, c is the conformation tensor representing the average of the end-to-end vector of the polymer molecules taken over all the molecules, p is the pressure field, $\boldsymbol{\tau}_p$ is the additional elastic stress tensor, $\beta = \eta_s/\eta_0$ with η_0 the solution dynamic viscosity and η_s the solvent contribution to the viscosity, $Re = \rho u_b h/\eta_s$ is the bulk mean Reynolds number, and $Wi = \lambda u_b/h$ is the Weissenberg number based on the

relaxation time λ of the viscoelastic fluid. The Peterlin function $f(r)$ is defined as

$$f(r) = (L^2 - 2)/(L^2 - r^2), \qquad (2.5)$$

where $r^2 = \text{tr}(\boldsymbol{c})$ is the trace of the conformation tensor $\boldsymbol{c}$, and L is the maximum extension length of FENE-P fluid.

2.2. *Numerical schemes*

The governing equations are solved based on the finite difference method using a DNS code developed in our previous work. The numerical code adopts a time-splitting method to solve the governing equations under a constant flow rate, which is conducted by the following four steps: (1) update the configuration tensor and calculate the elastic stress field by (2.3); (2) perform partial time marching of the velocity field containing convection, diffusion and elastic stress terms in (2.2) to obtain the first intermediate velocity field; (3) derive the pressure Poisson equation by substituting the first intermediate velocity field variable into (2.1), and solve it to obtain the second intermediate velocity with pressure terms; (4) maintain a constant flow rate by imposing an appropriate average pressure gradient on the second intermediate velocity. The above process solves the pressure field implicitly, and the time marching of other terms is solved by a second-order Adams–Bashforth scheme. More numerical details and validation can be found in Zhang *et al.* (2022, 2023).

It is worth highlighting our algorithm for handling the HWNP. The origin of the HWNP is closely related to the loss of the conformation tensor symmetric positive definite (SPD) property (Alves *et al.* 2021). Recently, we found that the improper interpolation methods of the conformation tensor are the main reason for losing its SPD property. Correspondingly, we proposed a tensor-based interpolation that is physically motivated (Zhang *et al.* 2023), instead of a component-based one to deal with the HWNP. The key to this method is to interpolate the eigenvalues and orientation of the conformation tensor $\boldsymbol{c}$ rather than its components. Comparing with traditional component-based methods, the accuracy of the conformation tensor invariants as well as its SPD property can be guaranteed at high Wi without adding any artificial diffusion. The application procedures are as follows.

(i) Decompose the conformation tensor field $\boldsymbol{c}$ as

$$\boldsymbol{c} = \boldsymbol{R}\boldsymbol{\Lambda}\boldsymbol{R}, \qquad (2.6)$$

$$\boldsymbol{\Lambda} = \begin{bmatrix} \Lambda_1 & 0 & 0 \\ 0 & \Lambda_2 & 0 \\ 0 & 0 & \Lambda_3 \end{bmatrix}, \qquad (2.7)$$

$$\boldsymbol{R} = \begin{bmatrix} \cos\theta\cos\varphi & \begin{array}{c}\sin\psi\sin\theta\cos\varphi \\ -\cos\psi\sin\varphi\end{array} & \begin{array}{c}\cos\psi\sin\theta\cos\varphi \\ +\sin\psi\sin\varphi\end{array} \\ \cos\theta\cos\varphi & \begin{array}{c}\sin\psi\sin\theta\sin\varphi \\ +\cos\psi\cos\varphi\end{array} & \begin{array}{c}\cos\psi\sin\theta\sin\varphi \\ -\sin\psi\cos\varphi\end{array} \\ -\sin\theta & \sin\psi\cos\theta & \cos\psi\cos\theta \end{bmatrix}, \qquad (2.8)$$

where ψ, θ and φ are Euler angles relative to the Cartesian coordinate system.

(ii) Given the known conformation tensor field $\boldsymbol{c}$, obtain the rotation matrix $\boldsymbol{R}$ and the diagonal matrix $\boldsymbol{\Lambda}$ by (2.5), and calculate the Eulerian angles and eigenvalues at the grid nodes.

(iii) Obtain the Eulerian angles ($\psi_{i+1/2}$, $\theta_{i+1/2}$, $\varphi_{i+1/2}$) and eigenvalues ($\Lambda_{1,i+1/2}$, $\Lambda_{2,i+1/2}$, $\Lambda_{3,i+1/2}$) at the grid interface through various interpolation schemes.

(iv) Calculate the diagonal matrix $\boldsymbol{\Lambda}_{i+1/2}$ and rotation matrix $\boldsymbol{R}_{i+1/2}$ at the grid interface by (2.7) and (2.8).

(v) Reconstruct the conformation tensor $\boldsymbol{c}_{i+1/2}$ at the grid interface by (2.6).

Moreover, to further improve the numerical accuracy, the above method can be combined with the high-order total variation diminishing schemes, such as the weighted essentially non-oscillatory (WENO) scheme used in this study. Taking the second-order WENO scheme (Shu 1998) as an example, the flux $H_{i+1/2}$ on the interface $i + 1/2$ can be calculated as

$$H_{i+1/2} = u_{i+1/2} f_{i+1/2}, \quad f_{i+1/2} = q_1 \times P_1 + q_2 \times P_2, \tag{2.9}$$

where $f_{i+1/2}$ is the interpolated variable on the interface $(i + 1/2)$ for $\Lambda_{i,i+1/2}$ and $\theta_{i,i+1/2}$, P_1 and P_2 are the results based on the second-order central and upwind interpolation templates, i.e. $P_1 = 1.5 f_C - 0.5 f_U$ and $P_2 = 0.5 f_C + 0.5 f_D$, and q_1 and q_2 are the smoothing factor of the two templates, i.e. $q_1 = 0.25/(10^{-6} + (f_U - f_C)^2)$ and $q_2 = 0.75/(10^{-6} + (f_U - f_C)^2)$. The subscripts U, C and D are the variables at the neighbour upstream, central and downstream nodes, respectively.

2.3. *Numerical conditions*

A series of simulations of the EIT state are conducted in a 2-D channel with varying dimensionless channel length *SX*, where $SX = 5n$, with $n = 0.5$, 1.0, 1.6, 2.0 and 4.0, respectively. In the existing studies (e.g. Dubief *et al.* 2022; Beneitez *et al.* 2024), a dimensionless channel length *SX* of 2π is frequently used, but there is no discussion on whether it can satisfy the MFU criterion. A wide range of *Wi* is covered, from 10 to 800, while keeping $Re = 2000$, $\beta = 0.9$ and $L^2 = 10\,000$. Linear stability analysis for FENE-P channel flow at the same condition indicates that centre mode instability occurs when *Wi* exceeds 150. However, despite the linear stability analysis predicting linear stability, DNS conducted by Shekar *et al.* (2020, 2021) demonstrate that EIT can indeed be excited at $Wi \geq 10$. Here, due to the use of different characteristic velocities to define *Wi*, the case $Wi = 10$ in our study corresponds to $Wi = 15$ in Shekar *et al.* (2020).

During the simulation, the grid is set to be non-uniform in the normal direction, and uniform in the streamwise direction. The grid in the normal direction is much denser near the wall and distributed as

$$y_j = \frac{1}{a} \tanh\left(\frac{1}{2} \delta_j \ln\left(\frac{1+a}{1-a}\right)\right), \tag{2.10}$$

where y_j is the location of the *j*th grid node, and $\delta_j = -1 + 2j/N_y$, with N_y the total grid number in the normal direction. After grid independence validation, the grid resolution is set to be $256n \times 304$, and the detailed validation is shown in the Appendix. The time step δt is set to be $5 \times 10^{-4} h/u_b$ or even smaller to achieve stable simulations. All the following simulations maintain for a sufficiently long duration to ensure statistical convergence and stability.
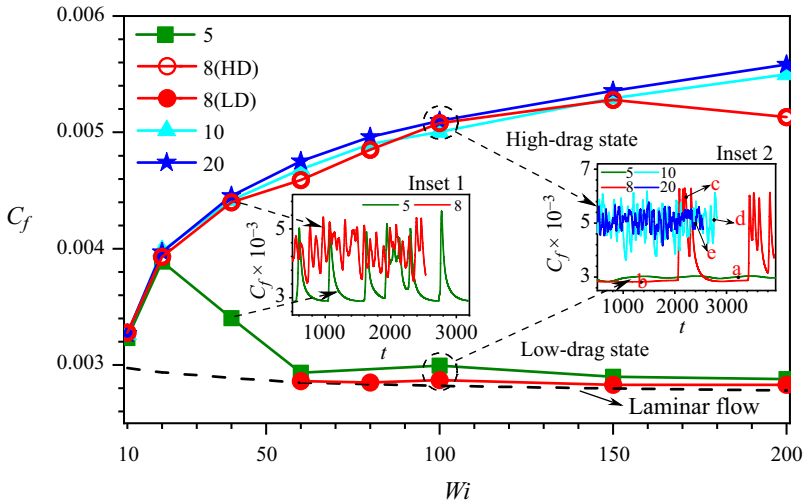
Figure 1. Temporally averaged and instantaneous C_f of viscoelastic fluid flow at different Wi obtained by different computational domains. The two insets are the instantaneous C_f at two typical Wi, 40 and 100, respectively. The red open and closed circles represent the temporally averaged C_f for different stable stages at $SX = 8$ under the same Wi value; LD indicates low-drag, and HD indicates high-drag. The dashed line corresponds to C_f in the laminar regime of FENE-P fluid at different Wi.

3. Results and analysis

3.1. *Computational domain effects on flow states*

First, the effects of the computational domain on flow states are evaluated through the statistical property, specifically the flow drag. Figure 1 illustrates the temporally averaged and instantaneous drag coefficient (C_f) of viscoelastic flows over a wide range of Wi obtained by different channel lengths. The two insets display the temporal evolution of the spatially averaged drag coefficient at two representative Wi values, 40 and 100. Therein, the symbols a–e in inset 2 are the typical moments of different channel length simulation cases, where a and b represent the low-drag states obtained by $SX = 5$ and 8, and c, d and e represent the high-drag states obtained by $SX = 8$, 10 and 20, respectively. It is evident that the choice of computational domain plays a crucial role in determining the numerically achieved flow states, particularly for cases of large Wi (e.g. above 40). When longer channels (e.g. $SX = 10$ and 20) are employed, the temporal evolution of C_f and flow structures demonstrate continuous occurrence of EIT, reaching a self-sustained state at $Wi > 10$. In these cases, the statistical drag coefficients converge as the channel length increases from $SX = 10$ to $SX = 20$. This indicates that a computation domain with $SX > 10$ is sufficient to capture the EIT state of FENE-P fluid for all presently considered Wi at $Re = 2000$, $\beta = 0.9$ and $L^2 = 10\,000$.

For the shorter channel lengths, such as $SX = 5$ and 8, the numerical results align with those of the longer channels at lower Wi (e.g. $Wi < 40$ for $SX = 5$, and $Wi < 60$ for $SX = 8$). However, as Wi is increased further, the flow alternates between a turbulent state with fluctuating high drag and a laminar-like state with stable low drag across a wide range of parameters. It is notable that the stable low-drag state (e.g. SAR state) discussed in this paper is not a turbulent state, different from active and hibernating turbulence proposed by Graham groups (Xi & Graham 2011; Xi & Bai 2016). Consequently, the statistical C_f decreases significantly, approaching levels seen in laminar flow (e.g. $Wi > 60$). In figure 1,
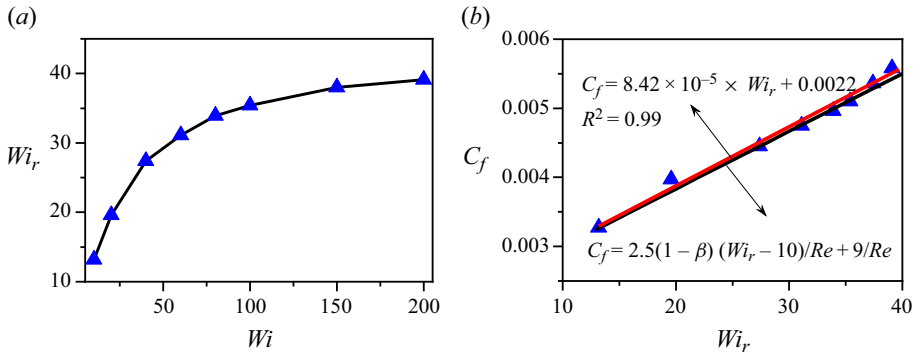
Figure 2. Relations of Wi_r with (*a*) Wi and (*b*) C_f.

red open and closed circles distinguish the drag coefficients of these two states at the same *Wi*. Interestingly, the averaged C_f in the high-drag state follows the scaling of EIT obtained from the longer channels, while the averaged C_f in the low-drag state approaches laminar flow. Through evaluating the detailed flow field, it is discovered that the low-drag state in these cases corresponds to the SAR state identified by Dubief *et al.* (2022), as illustrated in figure 4(*c*) later. Moreover, in the cases with $SX = 8$, both states exist intermittently for a certain duration (as shown in inset 2 of figure 1), while for $SX = 5$, the high-drag state immediately transitions to the low-drag state with increase of *Wi*. This suggests that the high-drag state cannot sustain continuously in a short channel, and a long channel is required to capture the EIT state.

It is worth noting that the intermittent flow state observed in the case with $SX = 8$ bears resemblance to the intermittent maintenance of laminar and turbulent states reported by Shekar *et al.* (2021). The influence of the computational domain on flow states mimics the effects of *Wi*. Here, the channel length $SX = 8$ is close to the critical length or the MFU to excite a continuous EIT state at $Wi > 60$. What is more, these findings obtained by changing the channel length at fixed L^2 also show great similarity to the effects of L^2 obtained by Dubief *et al.* (2022) at fixed channel length. Therein, they discovered that drag increase rises with increasing *Wi* under small L^2 conditions, then reaches a maximum value and subsequently decreases to zero (laminar flow) under large L^2 conditions. According to the above results, the effect observed in Dubief *et al.* (2022) can be explained as: large L^2 implies the existence of longer characteristic structures in EIT, which cannot be captured adequately by the shorter channel length. In other words, the decrease of drag increase or C_f with increasing *Wi* is caused by the insufficient channel length used in numerical simulations.

In our previous work, it was demonstrated that the nonlinear extension of the FENE-P model can affect the nature of the maximum drag reduction state, and the effective elasticity of FENE-P fluid related to L^2 is proposed to describe the coupling effect of nonlinear extension and local shear instead of *Wi* (Wang *et al.* 2021). Similarly, Wi_r is defined to characterize the average effective elastic effect on the flow as

$$Wi_r = \int_0^2 \overline{\frac{Wi}{f(r)} \frac{\partial u}{\partial y}} \, dy. \tag{3.1}$$

An interesting observation is that if we take into account the nonlinear extension effect of the FENE-P model, then the scaling of C_f with effective elasticity becomes simpler.
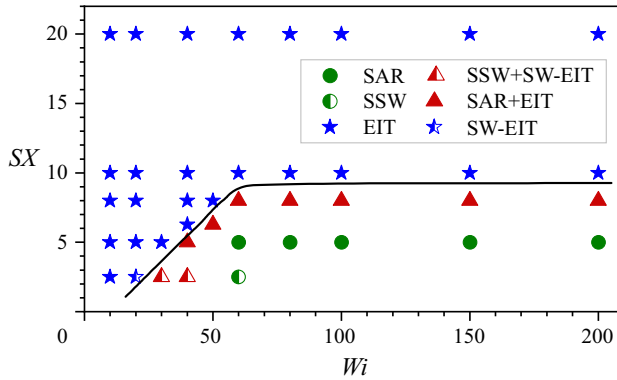
999 A82-8

Figure 3. Phase diagram of flow states at different *Wi* obtained by different computational domains. Here, SSW means steady sheets near the wall; SW-EIT means EIT occurrence near a single wall; '+' indicates the alternative occurrence of different states.

Figure 2 shows the relations of Wi_r with Wi and C_f, respectively. As is shown, Wi_r exhibits a behaviour similar to C_f in figure 1, and a linear function between C_f and Wi_r can be observed as shown in figure 2(*b*): $C_f \propto Wi_r$. This indicates that Wi_r is more suitable to describe the elastic effect in EIT, and the drag of EIT depends linearly on the effective elastic effect. Moreover, by evaluating this linear function, we can obtain an approximate scaling of C_f as $C_f \approx 2.5(1 - \beta)(Wi_r - 10)/Re + 9/Re \approx 8.42 \times 10^{-5} \times Wi_r + 0.0022$. The first term is related with the drag induced by EIT, and the second term is the drag of Newtonian laminar flow. This linear function agrees very well with the numerical data in the currently investigated parameter range of Wi ($10 \leq Wi \leq 200$, or $13 \lesssim Wi_r \lesssim 40$). It is certain that the scaling still needs further validation based on a large amount of numerical simulations under various conditions of varying Re and β in future work.

3.2. *The MFU of EIT*

According to the obtained drag coefficients and flow fields, figure 3 presents a phase diagram summarizing various viscoelastic flow states obtained from different computational domain sizes in a wide range of *Wi* (*Wi* > 10). The flow states depicted in the diagram are stable ones that can be sustained for sufficient periods. In figure 3, we supplement several cases of $SX = 2.5$ and 2π near the critical line to obtain the corresponding critical *SX* that can ensure stable EIT. Moreover, to have an intuitive image, the typical structures of different flow states are presented by the snapshots of polymer extension in figure 4. As mentioned above, the cases at all *Wi* considered in this paper are capable of reaching EIT if the channel is long enough. However, it is observed that with the increase of the channel length, the flow can experience several typical states, such as the SSW state with steady sheets near the wall, the SW-EIT state with EIT occurring near a single wall, the SAR state with steady arrowhead structure and EIT state. Except for EIT, these states may also be the solutions of governing equations or the attractors of FENE-P fluid channel flow, which are somehow unstable or appear only in a narrow parameter space.

Moreover, the phase diagram illustrated figure 3 allows us to identify the MFU required to produce the EIT state for different *Wi*. It is evident from the diagram that the size of the MFU increases with *Wi* and saturates when *Wi* exceeds a critical value (e.g. 60). Given the
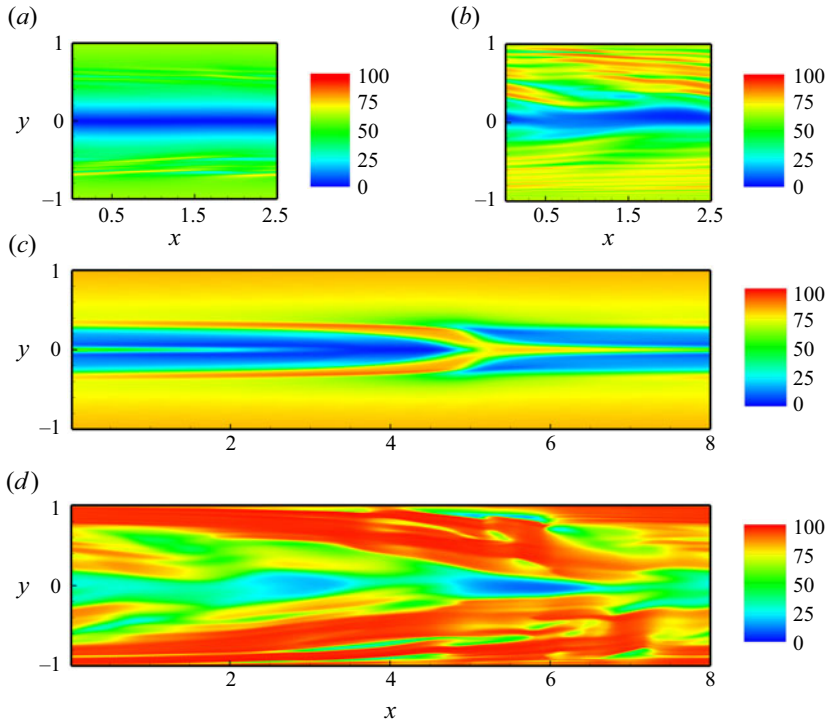
Figure 4. Features of different flow states: (*a*) SSW and (*b*) SW-EIT obtained at $Wi = 30$, $SX = 2.5$; (*c*) SAR and (*d*) EIT obtained at $Wi = 100$, $SX = 8$.

case of *Wi* above the critical value to excite EIT, if the computational domain is slightly shorter than the size of the MFU, then a switching phenomenon of EIT and SAR appears. Otherwise, EIT cannot be excited, and only SAR structures appear if the computational domain is too short. For example, when $Wi < 40$, a flow unit with size $SX > 5$ can achieve a self-sustained EIT state. However, for $Wi > 40$, a flow unit with $SX = 5$ is no longer able to sustain the EIT state, and instead exhibits a coexistence of SAR and EIT, or even a pure SAR state. Further increasing *Wi* above 60, a flow unit with $SX = 8$ also loses its ability to sustain the EIT state, and shows a coexistence of SAR and EIT. Notably, the flow unit with $SX = 10$ is sufficient to sustain EIT states for *Wi* ranging from 10 to 200 or even larger *Wi*, indicating a saturation of the effective elastic effect of FENE-P fluid at high *Wi*. Collecting the critical *SX* for different *Wi*, we give an approximate size of MFU required to sustain the EIT state in numerical simulations as $SX > f(Wi)$ for the parameters investigated in this study. This criterion can also be expressed as $SX > (0.65\,Wi_r - 10.66)$ in terms of Wi_r. Therefore, an appropriate size of the flow unit satisfying this criterion is suggested for the numerical simulation of EIT.

The above results clearly demonstrate the existence of an MFU for EIT to be self-sustained. This naturally raises the following questions. Why is a long channel required to produce EIT? What determines the MFU of EIT in numerical simulations? Answering these questions can give more insights into the origin and self-sustaining mechanism of EIT. Through evaluating the flow fields, it is observed the evolution process of sheet-like structures of polymer extension plays a crucial role in the generation and self-sustaining of EIT (see supplementary movies available at https://doi.org/10.1017/jfm.2024.977), which is in line with the findings in Shekar *et al.* (2021). Therefore, we
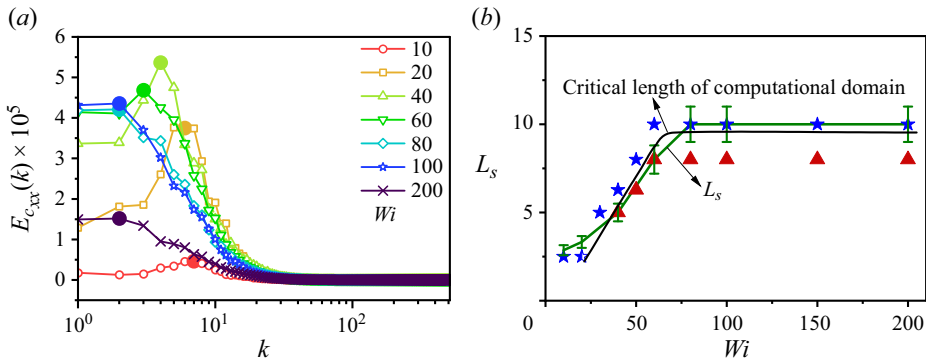
999 A82-10

Figure 5. (*a*) Spectra of the conformation tensor component c_{xx} at $y \approx 0.25$ at $SX = 20$ and different Wi, where the solid dots with different colours represent the peaks of the spectra. (*b*) Characteristic scales L_s of the c_{xx} and the critical computational domain at different Wi, where $L_s = 20/k_p$, and k_p is the peak wavenumber obtained from $E_{c_{xx}}(k)$. The stars and triangles represent the same flow patterns mentioned in figure 3, and the error bars represent $\pm 10\,\%$.

postulate that proper channel length to capture the evolution process of these structures is essential to sustain the EIT state. To test this hypothesis, we focus on the numerical results of cases obtained from a sufficiently large computational domain, $SX = 20$. Figure 5(*a*) illustrates the spectral characteristics of the conformation tensor component c_{xx} at different Wi. A peak in the low wavenumber can be observed near the wall at various Wi, corresponding to the number of the sheet-like structures in the channel of $SX = 20$. For example, when $Wi = 10$, the peak value $k_p = 7$ indicates that the characteristic length of the sheet-like extension structures or the spacing between two sheets is $SX/k_p \approx 3$. Additionally, figure 5(*b*) summarizes the relationship between the characteristic length of the sheets and Wi, which exhibits a consistent pattern with the critical MFU determined in figure 3. Based on these observations, we argue that the size of the MFU required for EIT is determined by the characteristic scale of the sheet-like structures.

3.3. *Dynamics of different flow states*

Based on the above results, this subsection explores the dynamics of different flow states. Figure 6 draws the dynamical and structural evolution of typical flow cases. Here, C_f and τ_{xx} characterize the energy dissipation and the energy stored in the polymers of channel flow, respectively. For the cases at $SX = 20$, it can be seen from the phase diagram that there are elliptical envelopes during the dynamical evolution of EIT, and the principal axes of the elliptical envelopes almost overlap under these conditions, which implies that the selected physical quantity can well describe the dynamics of EIT. For the channels with $SX = 8$, the envelope of dynamical evolution also has overlapping principal axes under low Wi conditions ($Wi < 40$). However, at high Wi, the flow shuttles back and forth between SAR and EIT. Starting from SAR, at first, C_f shows only a small increase, while τ_{xx} is significantly enhanced; subsequently, C_f shows a rapid increase and falls back to the EIT envelope line, while τ_{xx} is no longer significantly increased; finally, the flow falls back to SAR from the envelope line along the principal axis, and repeats the above process. Figure 6(*b*) focuses on the channel flows at $Wi = 100$. As SX increases, the flow undergoes the evolution process of pure SAR, intermittent flow regime between SAR and EIT, and fully developed EIT, respectively. The flow envelopes almost coincide under the conditions $SX = 10$ and $SX = 20$. This clearly demonstrates that the flow states obtained by insufficient channel length follow different dynamics from EIT.
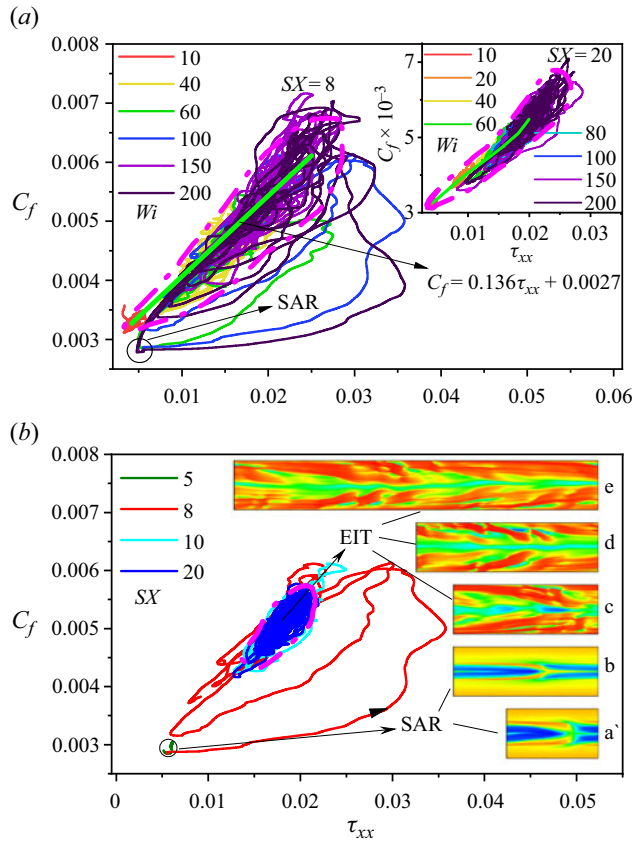
Figure 6. Dynamical and structural evolution cycles of C_f with τ_{xx} (a) for different Wi at $SX = 8$ and 20, (b) for different SX at $Wi = 100$ (the insets present the snapshots of streamwise extension fields c_{xx} for different SX, corresponding to the moments a–e in inset 2 of figure 1).

The above phenomenon can also be confirmed from the perspective of the stress balance, budgets of turbulent kinetic energy and elastic energy. The stress balance equation is obtained by the ensemble averaging of the momentum transport equation (2.2) as

$$\underbrace{-\overline{u'v'}}_{\overline{\tau_R}} + \underbrace{\frac{1-\beta}{Re\,Wi}(f(r)\,\overline{c_{xy}} - 1)}_{\overline{\tau_E}} + \underbrace{\frac{\beta}{Re}\frac{d\bar{u}}{dy}}_{\tau_V} = \underbrace{-\frac{dp}{dx}\left(1 - \frac{y}{h}\right)}_{\tau_T}, \tag{3.2}$$

where $\overline{(\cdot)}$ represents the ensemble-averaged variable, $(\cdot)'$ is the fluctuating variable, and $(\cdot)' = (\cdot) - \overline{(\cdot)}$. Here, τ_R, τ_E, τ_V and τ_T are the instantaneous Reynolds stress, elastic stress, viscous shear stress and total stress locally averaged along the streamwise, respectively. Similarly, the elastic energy budget equation can be obtained based on the elastic energy transport equation as

$$\int_0^2 \underbrace{\overline{\tau_E}\frac{\partial\bar{u}}{\partial y}}_{\overline{P_E}}\,dy - \int_0^2 \underbrace{\overline{\frac{f(r)\,\tau_{ii}}{2\,Wi}}}_{\overline{\varepsilon_E}}\,dy + \int_0^2 \underbrace{\overline{\tau'_{ij}\frac{\partial u'_i}{\partial x_j}}}_{\bar{R}}\,dy = 0, \tag{3.3}$$
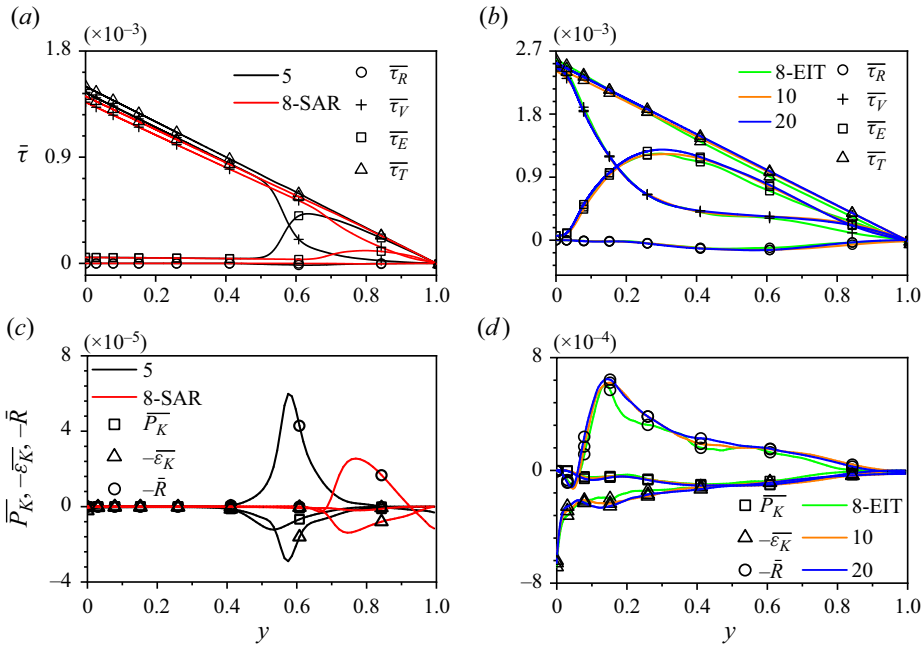
Figure 7. Statistical properties for different periods and channel lengths: (a,b) stress distributions in the normal direction based on inner scale; (c,d) turbulent kinetic energy budgets in the normal direction for different channels. Here, 8-SAR and 8-EIT correspond to the results obtained by $SX = 8$ in the SAR and EIT stages, respectively.

where P_E, ε_E and R are the instantaneous terms of the energy production by the elastic stress, the elastic dissipation, and energy exchange between elastic energy and turbulent kinetic energy locally averaged along the streamwise, respectively. Likewise, the budget of turbulent kinetic energy can be obtained as

$$\int_0^2 \underbrace{-\frac{1}{2}\overline{u'v'}\frac{\partial \bar{u}}{\partial y}}_{\overline{P_K}}\,\mathrm{d}y - \int_0^2 \underbrace{\frac{\beta}{Re}\overline{\frac{\partial u'_i}{\partial x_j}\frac{\partial u'_i}{\partial x_j}}}_{\overline{\varepsilon_K}}\,\mathrm{d}y - \int_0^2 \underbrace{\overline{\tau'_{ij}\frac{\partial u'_i}{\partial x_j}}}_{\bar{R}}\,\mathrm{d}y = 0, \tag{3.4}$$

where P_K and ε_K are the terms of the energy production by the Reynolds stress and the turbulent dissipation locally averaged along the streamwise direction, respectively.

Figure 7 illustrates the averaged budgets of shear stress and turbulent kinetic energy based on the results obtained by different channel lengths. Here, for the intermittent flow regime, the time averaging is performed for the different stages separately. As is shown, different flow patterns present completely different dynamical behaviour. The stage of SAR induced by the centre mode exhibits significant characteristics around the channel centre. For instance, the elastic nonlinear shear stress is lifted up with the peak close to the channel centre (see figure 7a). Although additional nonlinear shear stress is formed relative to laminar flow, it cannot cause a significant increase in flow drag due to the low shear strain rate therein. Compared to negative $\overline{P_K}$, turbulent kinetic energy comes from energy conversion term $\bar{R}$, which is also tightly supported near the channel centre (see figure 7d). However, unlike that of the SAR stage, the stage of EIT exhibits significant near-wall characteristics. For example, the peak of elastic nonlinear shear stress locates much closer to the wall compared to the SAR state (see figure 7b), which can induce

high flow drag weighted by high shear strain rate there. The formation of turbulent kinetic energy also relies mainly on energy conversion term $\bar{R}$, but the peak of $\bar{R}$ is very close to the wall. The above phenomena indicate that there exist completely different dynamic mechanisms for EIT from the flow pattern induced by the centre mode.

3.4. *Origin and self-sustaining process of EIT*

The intermittent flow regime between the SAR and EIT states provides a fabulous opportunity for exploring the origin and self-sustaining mechanism of EIT. To this end, this subsection investigates the structural and dynamical evolution processes of intermittent flow regime obtained at $Wi = 100$ with $SX = 8$, and $Wi = 40$ with $SX = 5$, respectively. The structural evolution is characterized by the polymer extension structures, and the dynamical evolution process is also evaluated using the the instantaneous budgets of turbulent kinetic energy and elastic energy, as well as shear stress balance analysis, respectively. For the two cases at $Wi = 100$ and 40, figures 8 and 9 show several typical moments of EIT from burst to disappearance. The detailed evolution can be found in the supplementary movies. As illustrated in figures 8 and 9 as well as the supplementary movies, the excitation process of EIT can be described as follows.

In the intermittent flow regime of $SX = 8$ and $Wi = 100$, starting from the flow with the SAR structure, several near-wall sheet-like streamwise extension structures first appear at $y \approx 0.5$ in the flow (see state 1). These structures gradually grow and extend towards the channel centre (see states 1 and 2). Then they begin to split and modulate the SAR structure (see states 3 and 4), until the SAR structure integrates into the sheet-like extension structures. Subsequently, frequent splitting leads to a rapid increase in C_f as shown in figure 6(a), then the flow develops into the EIT state without the SAR structure (see state 5). The detailed splitting process can be clearly identified in the supplementary movie of Case B from 21 s to 24 s. Due to the above demonstrated computational domain effects on flow states, EIT could not be maintained continuously for a long time as the near-wall extension structures gradually decline (see state 6). Finally, the flow returns to the SAR regime dominated by the centre mode (see state 7). After a long duration of the SAR state, the intervention of wall mode triggers the above process again.

Regarding the instantaneous dynamic evolution process, during the development process from pure SAR state to fully developed EIT state in figure 8, τ_E is significantly higher than τ_R, which is responsible for absorbing energy from the average motion and converting it into elastic energy, manifested as a significant elastic energy generation term P_E. However, the turbulent energy generation P_K is weaker, and even has a negative distribution in some regions. Turbulent velocity fluctuations come mainly from energy conversion R. The above phenomena indicate that elastic nonlinearity plays a dominant role in the dynamics of SAR and EIT, responsible for their induction and maintenance. Therefore, the origin and self-sustaining mechanism of EIT can be further confirmed by focusing on the elastic nonlinear behaviour in the flow. First, in the pure SAR state (state 7), the dynamic mechanism exhibits centralized characteristics in spatial distribution, such as the peak values of τ_E and P_E located at $y \approx 0.75$, and they are approximately linearly distributed at $y < 0.6$. Therefore, we believe that SAR is induced and maintained by the centre-mode dynamics. At state 1, with the burst of sheet-like extension structures, near-wall, wall-mode dynamics get involved in the flow, accompanied by local uplift of τ_E and P_E at approximately $y = 0.5$. Subsequently, the wall-mode dynamics gradually increases, and the modulated centre-mode dynamics becomes difficult to detect at state 2. In states 3 and 4, the wall-mode dynamics gradually shifts towards the channel wall with
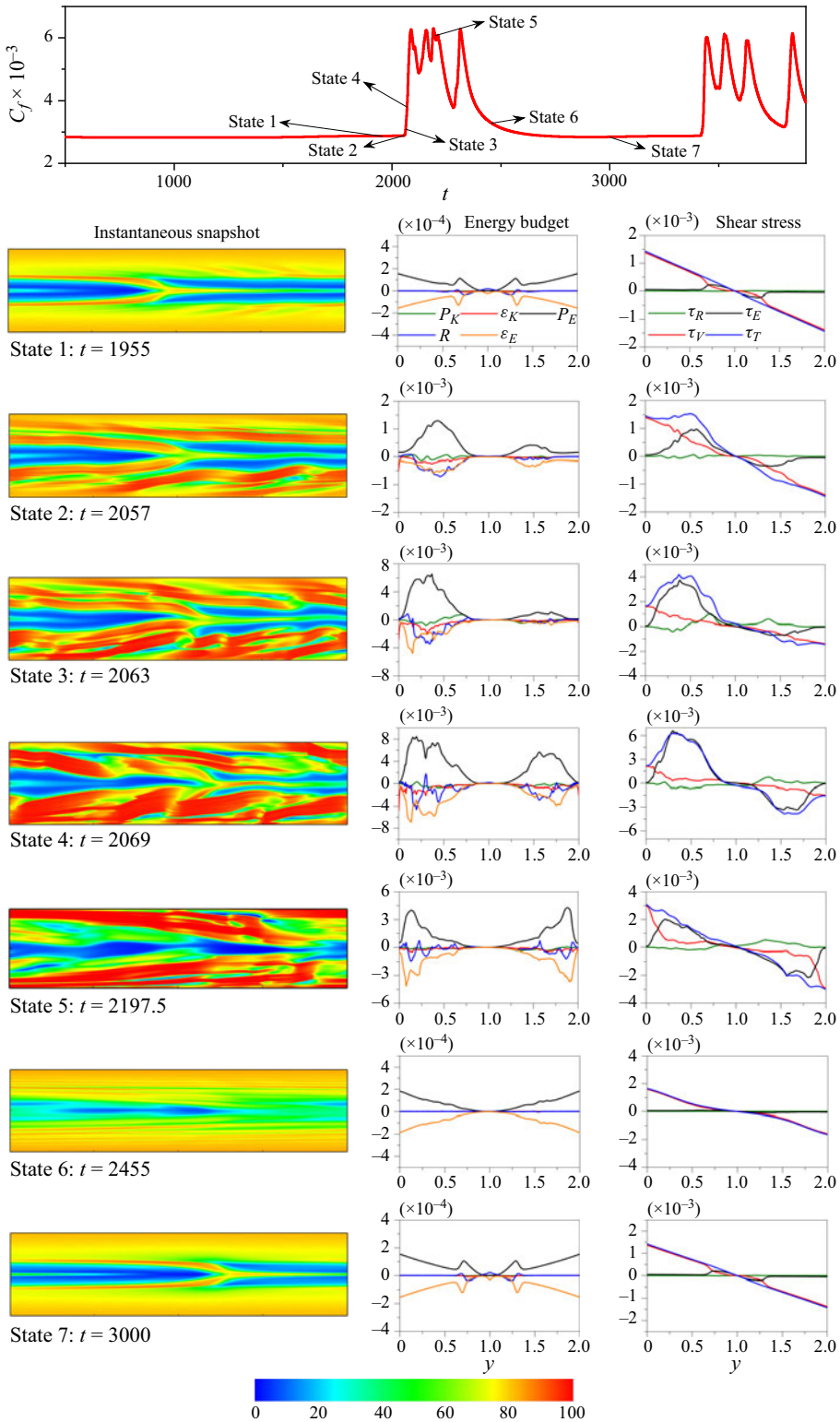
Figure 8. The structural and dynamical evolution processes of the intermittent flow regime at $Wi = 100$ and $SX = 8$.
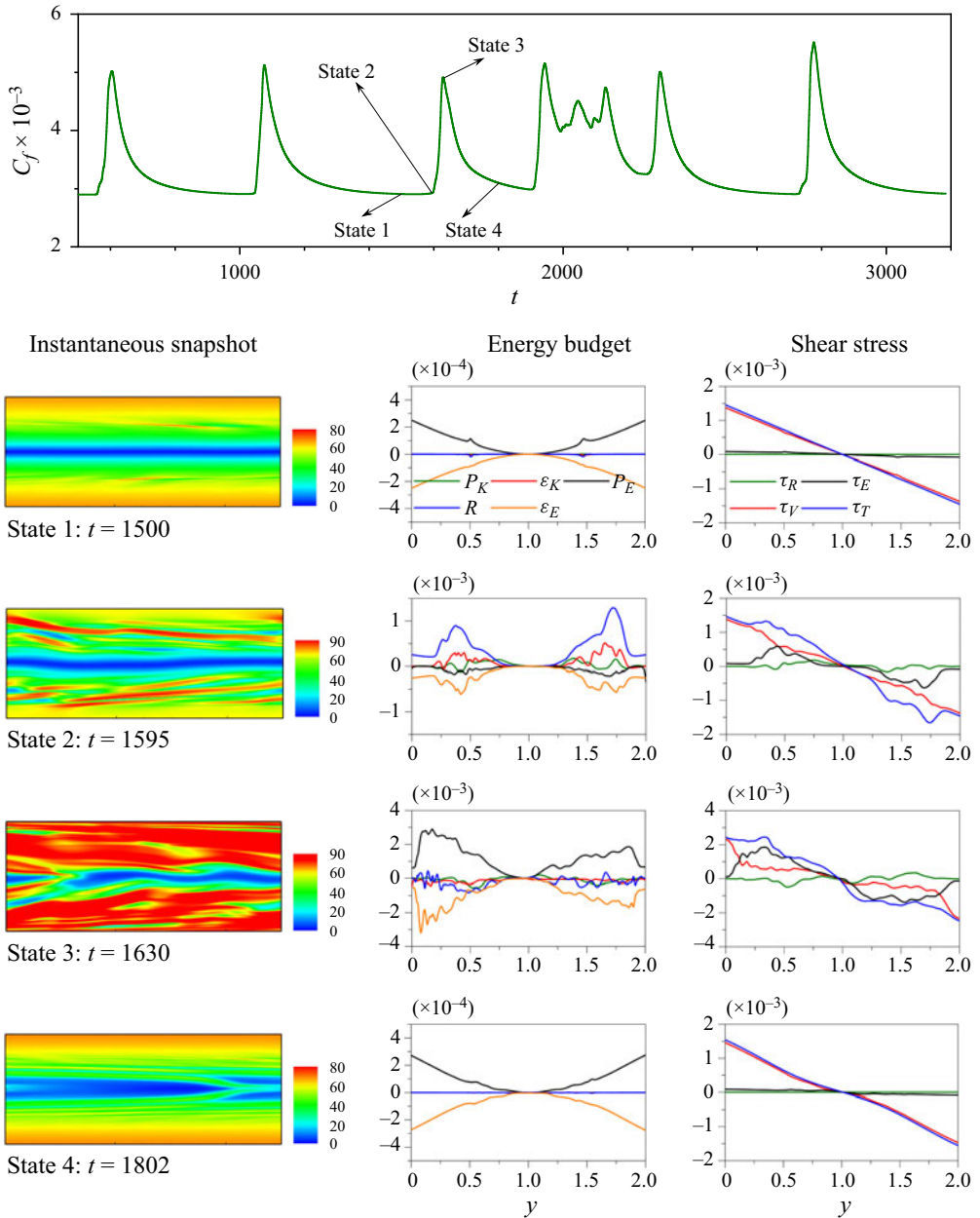
Figure 9. The structural and dynamical evolution processes of the intermittent flow regime at $Wi = 40$ and $SX = 5$.

high shear strain rates, causing a rapid increase in the flow drag. At state 5 with fully developed EIT, the wall-mode dynamics relatively decreases, and the peak values of τ_E and P_E are located at $y \approx 0.2$. It is interesting that at the moment when EIT decays to state 6, τ_E and P_E are extremely weak, and energy conversion almost disappears with the decay of EIT at state 6, which cannot provide energy for the maintenance of turbulent fluctuations, indicating the disappearance of elastic nonlinear dynamics. The above phenomena fully demonstrate that EIT originates not from the SAR structure induced by centre-mode dynamics, but rather from the sheet-like extension structures triggered by a wall mode.

Moreover, in the intermittent flow regime of $SX = 5$ and $Wi = 40$, as shown in figure 9, it is observed that even starting from the laminar-like flow without SAR structure, the appearance and evolution of near-wall sheet-like structures still closely mirror the process of the case at $SX = 8$, $Wi = 100$ in figure 8. They trigger the flow to be unstable and EIT state finally (see state 3). This detailed process can be found in the supplementary movie of Case A from 18 s to 28 s. Similar processes can also be confirmed through the evolution of instantaneous dynamics in figure 9 from state 1 to state 4. Here, the non-existence of peaks near the centreline further corroborates the absence of centre mode.

Therefore, the above results indicate that in the current parameter space, the EIT originates from the near-wall sheet-like structures induced by some wall modes rather than the centre mode, no matter whether there exists centre mode instability or not. From the perspective of dominant structure regeneration, the self-sustaining process of EIT can be described as: small disturbances near the wall induce high extension sheet-like structures, which gradually grow and split under the elastic nonlinearity as well as the fluid inertia, and regenerate new sheet-like structures. The above process continues to occur, maintaining the turbulent state of the flow. Therefore, different from the process of large eddies generating small eddies, and small eddies generating mini eddies in IT, we argue that there exists a different type of structural similarity in EIT: large extension sheets generate small extension sheets, and small extension sheets continues to regenerate as they grow.

4. Concluding remarks

In summary, a series of DNS of 2-D channel FENE-P fluid flow is performed to obtain the MFU of EIT in this paper. Based on the numerical results, the origin and self-sustaining process of EIT are then investigated, and the following major conclusions can be drawn.

(1) The size of the computational domain can significantly affect the numerically obtained flow pattern. The improper choice of domain size will lead to different or inaccurate flow dynamics. If the channel length is long enough, then the flow will sustain the EIT regime with the increase of Wi; otherwise, the flow will gradually fall back from the EIT state to the SAR state due to the insufficient channel length. This implies the existence of an MFU to sustain the EIT state. Moreover, it is found that the MFU is essentially determined by the characteristic scale of polymer extension structures whose evolution is crucial to the sustenance of EIT.

(2) Through investigating the dynamics of different flow states, it is found that the flow states obtained by insufficient channel length follow different dynamics from EIT. The SAR state exhibits dominant dynamics near the channel centre. Unlike the SAR state, EIT shows significant near-wall features, with the peak of elastic nonlinear shear stress and the energy exchange between elastic energy and turbulent kinetic energy located near the wall.

(3) The intermittent flow regime obtained at the critical channel length gives an in-depth insight on the origin and sustaining process of EIT. It indicates that in the absence of SAR structures, the sheet-like extension structures near the wall can be induced and gradually evolve into fully developed EIT. This means that EIT originates not from the centre mode, but from some wall modes, which induces the sheet-like extension structures near the wall. In detail, the sheet-like extension structures induced by small disturbances gradually grow and fracture, while the extension structures formed by fractures continue to grow and fracture. Once triggered, EIT is self-sustained by the regeneration of the extension structures.

So far, the above results are obtained under fixed inertial effect, and comprehensive investigations are of course still necessary to draw an exhaustive picture of an MFU
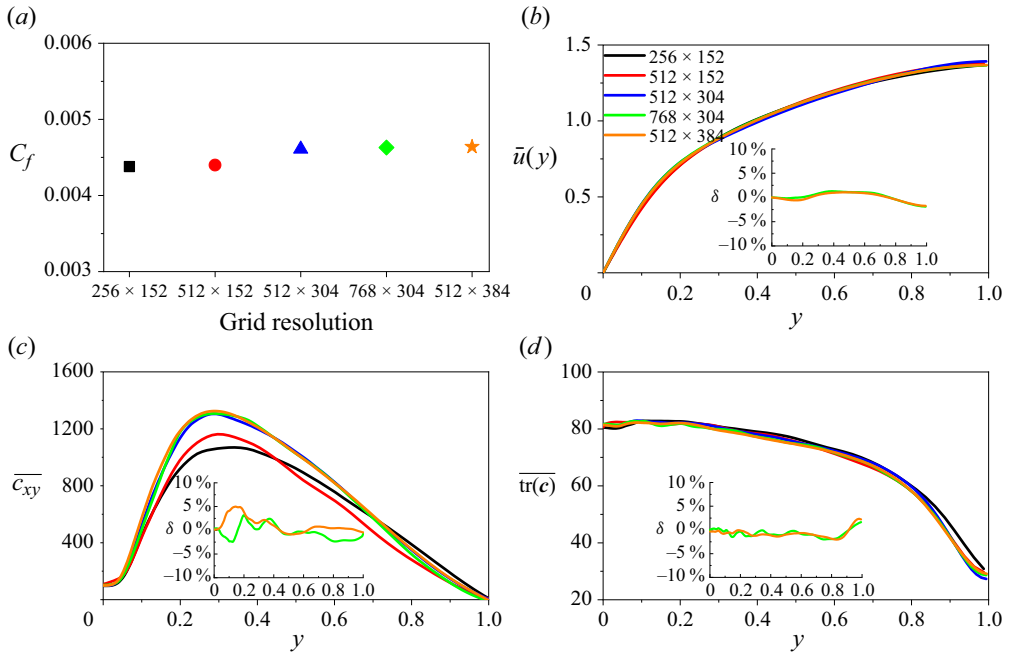
Figure 10. Statistics obtained by different grid resolutions for the case $Re = 2000$, $\beta = 0.9$, $L^2 = 10\,000$, $Wi = 60$: (a) the ensemble-averaged drag coefficient C_f; (b) the profile of the mean streamwise velocity $\bar{u}$; (c) the profile of $\overline{C_{xy}}$; (d) the profile of $\overline{\mathrm{tr}(c)}$. Here, $C_f = 2\overline{\tau_w}/\rho u_b^2$ with $\overline{\tau_w}$ is the temporally averaged wall shear stress. The insets illustrate the relative differences δ of the results at the 512×304 grid comparing with those of higher resolution cases (768×304 and 512×384, respectively).

for EIT. Moreover, with the MFU, now we can reach the level of identification of various exact coherent structures, the geometry of EIT, and detailed dynamical process of EIT in future work.

Author ORCID.
Hongna Zhang https://orcid.org/0000-0002-1161-0897.

Appendix

Before a large amount of numerical simulation, grid independence validation was conducted at two representative Wi values (i.e. $Wi = 60$ and 100) and different channel lengths. Figures 10 and 11 illustrate some important statistics and structural properties obtained under different grid sets at $Wi = 60$, $SX = 10$. The insets illustrate the relative differences δ of the results at the 512×304 grid, comparing with those at higher-resolution cases (768×304 and 512×384), respectively. Here, the relative differences at different grid resolutions are defined as $\delta = (\theta_i - \theta_{512\times304})/\theta_{512\times304,p}$, where θ_i represents the results at higher resolution, $\theta_{512\times304}$ represents the results at the 512×304 grid, and $\theta_{512\times304,p}$ represents the peak value of the corresponding data. It can be found that
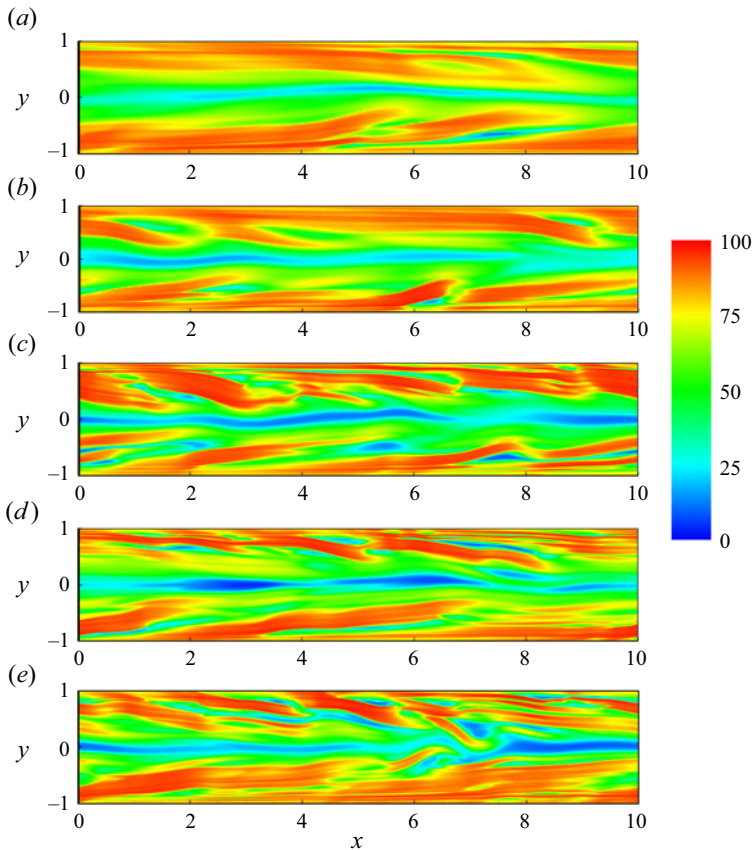
999 A82-18

Figure 11. Instantaneous snapshots of polymer extension obtained by different grid resolutions: (*a*) 256×152, (*b*) 512×152, (*c*) 512×304, (*d*) 768×304, (*e*) 768×384.

the variation of the streamwise grid number from $N_x = 256$ to $N_x = 768$ has gradually decreasing effects on the statistics and the structural properties, and the results converge at $N_x = 512$. Fixing $N_x = 512$, with the increase of grid resolution in the normal direction from $N_y = 152$ to $N_y = 384$, the statistics of EIT increase slightly and almost converge at $N_y = 304$. With the 512×304 grid, the numerical simulations can accurately predict no matter the tendency but also the peaks of different parameters. As illustrated by the insets of figure 10, the relative differences of different parameters are mostly less than 1 %, and the maximum ones are within 5 %, comparing with those at the two highest resolution cases. Furthermore, figure 12 shows the energy spectrum at different locations for the case with resolution 512×304 and $Wi = 60$, which proves that there is no energy accumulation at a higher wavenumber region. Therefore, the grid resolution 512×304 is suitable in the current study.

Moreover, figure 13 shows the grid effects on the obtained flow pattern under different channel lengths at a relatively high Wi ($Wi = 100$). As is shown, the improper choice of grid resolution can produce different flow states. For instance, at $Wi = 100$, $SX = 5$, the flow state obtained by the 128×152 grid is an intermittent chaotic state with higher drag, but it converges to a steady state with an arrowhead structure and much lower drag when refining the grid to be 224×272, 256×304 and further finer grids. Here, it seems to
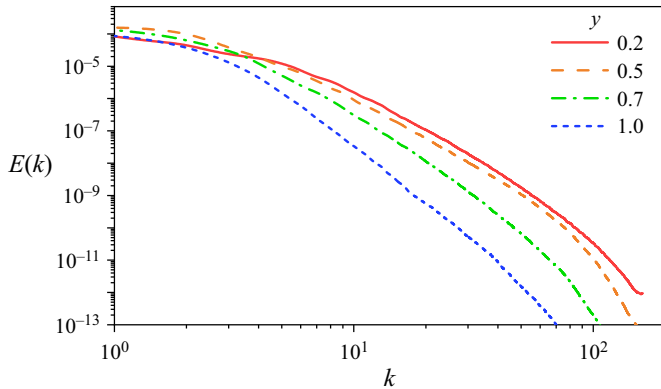
999 A82-19

Figure 12. Energy spectrum $E(k)$ at different locations for $Re = 2000$, $\beta = 0.9$, $L^2 = 10\,000$ and $Wi = 60$ with the 512×304 grid.
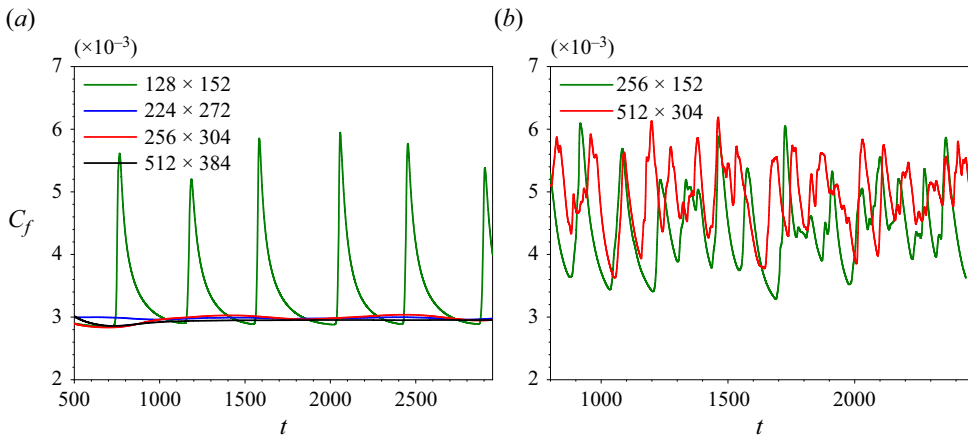

Figure 13. Comparison of instantaneous C_f for cases with different lengths and grid resolutions for $Re = 2000$, $\beta = 0.9$, $L^2 = 10\,000$, $Wi = 100$.

be counter-intuitive that a more chaotic state is obtained at a coarser grid, which may be related to the PDI. Insufficient grid resolution, which brings in an additional numerical artificial diffusion, can lead to new type of non-physical flow instability. The increase of grid resolution can alleviate this non-physical flow instability. Finally, to get converged results, the grid resolution is set to be $256n \times 304$ during all the simulations.

REFERENCES

ALVES, M.A., OLIVEIRA, P.J. & PINHO, F.T. 2021 Numerical methods for viscoelastic fluid flows. *Annu. Rev. Fluid Mech.* **53**, 509–541.

BENEITEZ, M., PAGE, J., DUBIEF, Y. & KERSWELL, R.R. 2024 Multistability of elasto-inertial two-dimensional channel flow. *J. Fluid Mech.* **981**, A30.

BENEITEZ, M., PAGE, J. & KERSWELL, R.R. 2023 Polymer diffusive instability leading to elastic turbulence in plane Couette flow. *Phys. Rev. Fluids* **8**, L101901.

CHOUEIRI, G.H., LOPEZ, J.M. & HOF, B. 2018 Exceeding the asymptotic limit of polymer drag reduction. *Phys. Rev. Lett.* **120**, 124501.

CHOUEIRI, G.H., LOPEZ, J.M., VARSHNEY, A., SANKAR, S. & HOF, B. 2021 Experimental observation of the origin and structure of elastoinertial turbulence. *Proc. Natl Acad. Sci. USA* **118** (45), e2102350118.

COUCHMAN, M.M.P., BENEITEZ, M., PAGE, J. & KERSWELL, R.R. 2024 Inertial enhancement of the polymer diffusive instability. *J. Fluid Mech.* **981**, A2.

DUBIEF, Y., PAGE, J., KERSWELL, R.R., TERRAPON, V.E. & STEINBERG, V. 2022 First coherent structure in elasto-inertial turbulence. *Phys. Rev. Fluids* **7**, 073301.

DUBIEF, Y., TERRAPON, V.E. & HOF, B. 2023 Elasto-inertial turbulence. *Annu. Rev. Fluid Mech.* **55**, 675–705.

DUBIEF, Y., TERRAPON, V.E. & JULIO, S. 2013 On the mechanism of elasto-inertial turbulence. *Phys. Fluids* **25**, 110817.

GARG, P., CHAUDHARY, I., KHALID, M., SHANKAR, V. & SUBRAMANIAN, G. 2018 Viscoelastic pipe flow is linearly unstable. *Phys. Rev. Lett.* **121**, 024502.

GRAHAM, M.D. 2014 Drag reduction and the dynamics of turbulence in simple and complex fluids. *Phys. Fluids* **26** (10), 101301.

GROISMAN, A. & STEINBERG, V. 2000 Elastic turbulence in a polymer solution flow. *Nature* **405** (6782), 53–55.

GROISMAN, A. & STEINBERG, V. 2004 Elastic turbulence in curvilinear flows of polymer solutions. *New J. Phys.* **6** (1), 29.

JIMÉNEZ, J. & MOIN, P. 1991 The minimal flow unit in near-wall turbulence. *J. Fluid Mech.* **225**, 213–240.

KHALID, M., CHAUDHARY, I., GARG, P., SHANKAR, V. & SUBRAMANIAN, G. 2021 The centre-mode instability of viscoelastic plane Poiseuille flow. *J. Fluid Mech.* **915**, A43.

LI, F.C., YU, B., WEI, J.J. & KAWAGUCHI, Y. 2012 *Turbulent Drag Reduction by Surfactant Additives*. John Wiley & Sons.

PAGE, J., DUBIEF, Y. & KERSWELL, R.R. 2020 Exact travelling wave solutions in viscoelastic channel flow. *Phys. Rev. Lett.* **125**, 154501.

SAMANTA, D., DUBIEF, Y., HOLZNER, M., SCHAFER, C., MOROZOV, A.N., WAGNER, C. & HOF, B. 2013 Elasto-inertial turbulence. *Proc. Natl Acad. Sci. USA* **110**, 10557.

SÁNCHEZ, H.A.C., JOVANOVIĆ, M.R., KUMAR, S., MOROZOV, A., SHANKAR, V., SUBRAMANIAN, G. & WILSON, H.J. 2022 Understanding viscoelastic flow instabilities: Oldroyd-B and beyond. *J. Non-Newtonian Fluid Mech.* **302**, 104742.

SHEKAR, A., MCMULLEN, R., MCKEON, B. & GRAHAM, M. 2020 Self-sustained elastoinertial Tollmien–Schlichting waves. *J. Fluid Mech.* **897**, A3.

SHEKAR, A., MCMULLEN, R.M., MCKEON, B.J. & GRAHAM, M.D. 2021 Tollmien–Schlichting route to elastoinertial turbulence in channel flow. *Rev. Fluids* **6**, 093301.

SHEKAR, A., MCMULLEN, R.M., WANG, S.N., MCKEON, B.J. & GRAHAM, M.D. 2019 Critical-layer structures and mechanisms in elastoinertial turbulence. *Phys. Rev. Lett.* **122**, 124503.

SHU, C. 1998 Essentially non-oscillatory and weighted essentially non-oscillatory schemes for hyperbolic conservation laws. In *Advanced Numerical Approximation of Nonlinear Hyperbolic Equations* (ed. A. Quarteroni), pp. 325–432. Springer.

SID, S., TERRAPON, V.E. & DUBIEF, Y. 2018 Two-dimensional dynamics of elasto-inertial turbulence and its role in polymer drag reduction. *Phys. Rev. Fluids* **3**, 011301.

STEINBERG, V. 2021 Elastic turbulence: an experimental view on inertialess random flow. *Annu. Rev. Fluid Mech.* **53**, 27–58.

TOMS, B.A. 1949 Some observations on the flow of linear polymer solutions through straight tubes at large Reynolds numbers. In *Proc. 1st International Congress on Rheology*, vol. 2, pp. 135–141. North-Holland.

WAN, D.D., SUN, G.R. & ZHANG, M.Q. 2021 Subcritical and supercritical bifurcations in axisymmetric viscoelastic pipe flows. *J. Fluid Mech.* **929**, A16.

WANG, S.M., ZHANG, W.H., WANG, X.Y., LI, X.B., ZHANG, H.N. & LI, F.C. 2021 Maximum drag reduction state of viscoelastic turbulent channel flow: marginal inertial turbulence or elasto-inertial turbulence. *J. Fluid Mech* **960**, A12.

WHITE, C.M. & MUNGAL, M.G. 2008 Mechanics and prediction of turbulent drag reduction with polymer additives. *Annu. Rev. Fluid Mech.* **40**, 235–256.

XI, L. & BAI, X. 2016 Marginal turbulent state of viscoelastic fluids: a polymer drag reduction perspective. *Phys. Rev. E* **93**, 043118.

XI, L. & GRAHAM, M.D. 2010 Turbulent drag reduction and multistage transitions in viscoelastic minimal flow units. *J. Fluid Mech.* **647**, 421–452.

XI, L. & GRAHAM, M.D. 2011 Active and hibernating turbulence in minimal channel flow of Newtonian and polymeric fluids. *Phys. Rev. Lett.* **104**, 218301.

YIN, G., HUANG, W.X. & XU, C.X. 2018 Prediction of near-wall turbulence using minimal flow unit. *J. Fluid Mech.* **841**, 654–673.

ZHANG, H.N., ZHANG, W.H., WANG, X.Y., LI, Y.S., MA, Y., LI, X.B. & LI, F.C. 2023 On the role of tensor interpolation in solving high-Wi viscoelastic fluid flow. *Phys. Fluids* **35**, 031708.

ZHANG, W.H., ZHANG, H.N., WANG, Z.M., LI, Y.K., YU, B. & LI, F.C. 2022 Repicturing viscoelastic drag-reducing turbulence by introducing dynamics of elasto-inertial turbulence. *J. Fluid Mech.* **940**, A31.

ZHU, L. & XI, L. 2021 Nonasymptotic elastoinertial turbulence for asymptotic drag reduction. *Phys. Rev. Fluids* **6**, 014601.